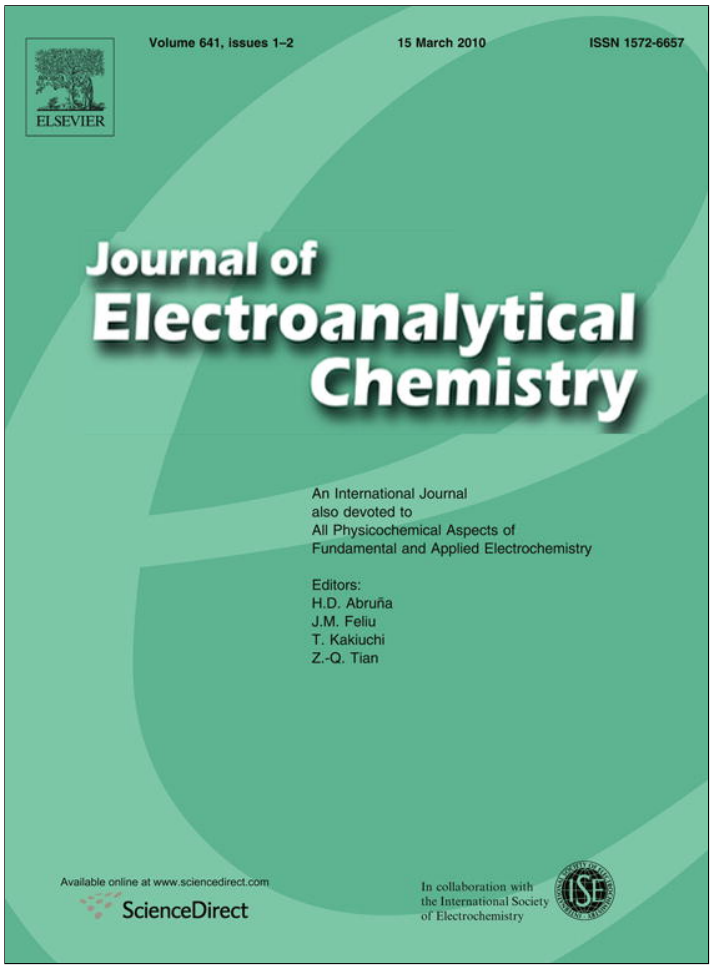

Journal of Electroanalytical Chemistry 641 (2010) 119–130

Contents lists available at ScienceDirect

Journal of Electroanalytical Chemistry

journal homepage: www.elsevier.com/locate/jelechem

A comparative study of the oxygen evolution reaction on oxidised nickel, cobalt and iron electrodes in base

Michael E.G. Lyons *, Michael P. Brandon

Physical and Materials Electrochemistry Laboratory, School of Chemistry, University of Dublin, Trinity College, Dublin 2, Ireland

ARTICLE INFO

Article history:
Received 11 March 2009
Received in revised form 28 August 2009
Accepted 17 November 2009
Available online 7 January 2010

Keywords:
Oxygen evolution
Tafel slope
Dual barrier model
Iron electrode
Cobalt electrode
Nickel electrode

ABSTRACT

Despite the recent renewal in interest in the oxygen evolution reaction (OER) at transition metal oxide based electrodes in alkaline solution, the details of the mechanism remain controversial. While most studies focus on a particular oxide in isolation, a consistent experimental examination of the oxides of adjacent elements is likely to be fruitful with respect to mechanistic elucidation. In the present comprehensive work, the kinetics of the OER proceeding on the anodic passive oxides of iron, cobalt and nickel are probed using steady state polarisation to ascertain values of the Tafel slope, b, and the OH^- ion reaction order, m_{OH^-}. The critically important matter of the interplay between the observed OER kinetic parameters and the electrochemistry and structure of the underlying oxide, is explored using cyclic voltammetry. Tafel slopes of $b \approx 46$ mV dec^{-1} observed for pre-reduced Fe and Co anodes, are rationalised on the basis of a "barrier oxide" associated with the inner anhydrous region of the passive film. A reaction path involving the rate determining formation of a superoxy (—OOH) intermediate is proposed. A meaningful comparison of the catalytic performances of the oxides is facilitated by the estimation of active surface areas, using a transient decay measurement technique.

1. Introduction

Alkaline water electrolysis, using electricity generated by renewable sources has been proposed as an environmentally inoffensive route to the production of the large volumes of hydrogen gas required by a possible hydrogen economy. In practice the efficiency of water electrolysis is limited by the large anodic overpotential of the oxygen evolution reaction (OER) [1]. Over the past thirty years, considerable research effort has been devoted to the design, synthesis and characterisation of anode materials, with the aim of achieving useful rates of the OER at the lowest possible overpotential, in order to optimise the overall electrolysis process.

At practical current densities, anodes of RuO_2 or IrO_2 exhibit the lowest OER overpotentials, however these oxides suffer from poor chemical stability in alkaline media [2]. The oxides of first row transition metals, in particular nickel and cobalt, offer a compromise solution – although they possess inferior electrocatalytic activity for the OER, they display excellent long term corrosion resistance in aqueous alkaline solution and have the added advantage of being relatively inexpensive [1–3]. In view of this, nickel hydroxides [1,4–6], spinels (ABO_3) including Co_3O_4 [7–10], $NiCo_2O_4$ [11–14] and various ferrites [15,16], perovskites (ABO_3, A is a lanthanide, B is a first row transition metal) [17–20], and transition metal based amorphous alloys [21–23] have all been proposed for OER anode applications. The aforementioned oxides were prepared from inorganic precursor materials using a wide variety of approaches, including, thermal decomposition, spray pyrolysis, sol–gel routes and freeze drying, precipitation or electro-deposition from solution. Refs. [4–23] are randomly chosen examples, representative of a much larger body of relatively recent literature on the optimisation of OER anode materials. Despite all this work, the mechanism of the OER at first row transition metal oxide surfaces remains controversial and the question of a possible common mechanism (which would facilitate a theory of electrocatalysis for oxygen evolution) is therefore unresolved.

At a more fundamental level, oxygen evolution also proceeds at the surface of the anodic oxides that passivate transition metal electrodes in alkaline solution, albeit (generally) at somewhat greater overpotentials relative to the specifically prepared oxides discussed above. It is our opinion that a systematic and consistent study of the OER at the oxidised surfaces of electrodes of adjacent first row transition metals should prove useful in elucidating whether a common reaction mechanism prevails, and if so, which (if any) of the previously proposed pathways is most likely. Polycrystalline nickel anodes have been commercially utilised in water electrolysis and consequently there exists a significant body of work on this system [24–32]. In contrast, we are aware of only three separate studies [33–36] on the OER at oxidised cobalt electrodes, while our own work [37,38] is, to the best of our

* Corresponding author. Tel.: +353 1 8962051; fax: +353 1 6712826.
E-mail address: melyons@tcd.ie (M.E.G. Lyons).

1572-6657/$ - see front matter © 2010 Elsevier B.V. All rights reserved.
doi:10.1016/j.jelechem.2009.11.024

knowledge, the only published account of the reaction at oxidised iron anodes. An early comparative study of oxygen evolution at Ni, Pt, Co, Fe and several alloy electrodes was provided by Scarr [39], however the analysis was solely based on measured values of the OER Tafel slope, b, and exchange current density, i_0. In the present article we expand upon the scope of Scarr's work, for oxidised Ni, Co and Fe electrodes, by obtaining reaction order data (with respect to OH^- ion activity) to complement Tafel slope measurements. Furthermore, the interplay between anodic oxide electrochemistry (as characterised by cyclic voltammetry) and OER catalytic performance, is explored in an attempt to understand why oxygen evolution kinetic parameters vary with electrode age and/or pre-treatment regime. The difficult issue of active surface area evaluation for anodic oxide covered electrodes is also confronted, in order to facilitate a meaningful comparison of the relative catalytic activities of the electrodes for the OER.

2. Experimental

The preparation of the working electrodes from pure polycrystalline samples (>99.9%, metals basis) of the relevant metal has been described elsewhere [38,40], along with details of the sourcing of these metals. It is worth commenting that the Ni and Fe electrodes were prepared from foils (exposed apparent surface area = 0.16 cm^2), while the Co anode was prepared from a wire (exposed apparent cross sectional area = ~0.0314 cm^2). In the course of the text, various pre-treatment regimes will be briefly outlined – however prior to each experiment, before any electrochemical pre-treatment, all electrodes were polished to a mirror finish using a slurry of 0.05 μm alumina powder.

Sodium hydroxide (BDH AnalaR®, minimum 98% purity) solutions made up in Millipore water (resistivity 18 MΩ cm) served as the electrolyte. The OH^- ion activity, a_{OH^-} a_{OH^-}, for each solution was evaluated on the basis of the literature value [41] for the mean ionic activity coefficient, $\gamma_{\pm}$, for a NaOH solution of that concentration. All experiments were conducted at room temperature. A standard three electrode cell arrangement was utilised except in roughness factor estimation experiments. The reference electrode was a mercury–mercuric oxide (Hg/HgO, 1 M NaOH) electrode (Radiometer Analytical – cat No. XR400), which has a potential of +0.098 V vs. the standard hydrogen electrode in a solution of pH 14 at 25 °C. A platinum wire served as the counter electrode.

The experiments were performed using a PC controlled Zahner Elektrik IM6 unit. Polarisation data was obtained by changing the potential, step-wise (5 mV steps) in the positive direction, with sufficiently long delays to achieve the steady state. The electrolyte resistance was quantified using the impedance method, which permitted all polarisation plots to be corrected for the iR drop. Except where otherwise stated, all values of current density are quoted with respect to the geometric (apparent) electrode surface area.

For each electrode, the active surface area for oxygen evolution was estimated using the so-called OH_{ads} desorption method, pioneered by Ho and Piron [42,43]. The basic measurement circuit is depicted schematically in Fig. 1. The current source was the IM6 unit in galvanostatic mode, while the oscilloscope was a Velamen PCS100 PC controlled digital storage oscilloscope.

The technique involved the charging (circuit a of Fig. 1) of the working electrode at an anodic current density, i_{appl}, corresponding to the OER proceeding in the steady state. When the polarisation was interrupted by throwing the relay switch to circuit b, the electrode discharged to ground through the 1 Ω series resistance. According to Ohms law, for a 1 Ω resistor, the oscilloscope trace effectively maps the decay current–time (i_{dec}–t) transient. The quantity of interest was the total cathodic charge, Q_{dec}, passed during the decay – this was evaluated by integrating the oscilloscope

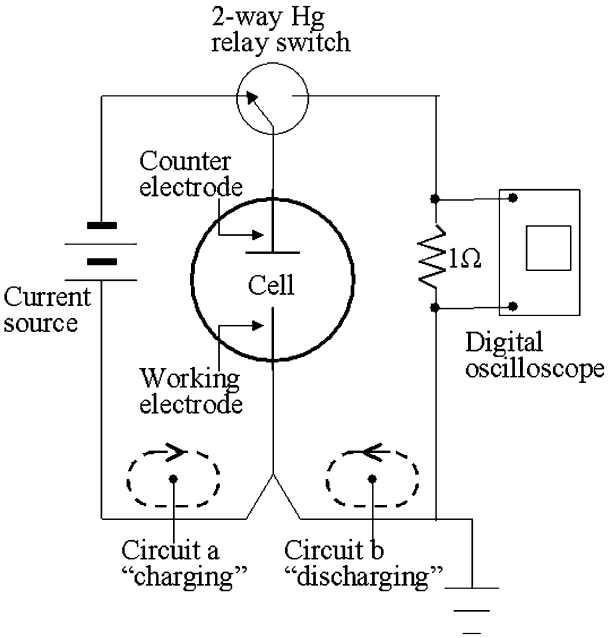

Fig. 1. Schematic of the circuitry used in active surface area estimation by the OH desorption method.

i_{dec}–t trace between t = 0, and the time at which the decay current became zero. This process was repeated for a number of values of i_{appl}, derived from the steady state $i(E)$ characteristic for the system under study, thus enabling the construction of a Q_{dec} vs. E plot for each anode, as in Fig. 10, Section 5. The period of charging for a given i_{appl} was determined in a prior galvanostatic experiment with the normal three electrode cell, as the time required for the steady state potential to become established following the imposition of i_{appl} at open circuit.

3. Results

3.1. Nickel: voltammetry and steady state polarisation

The data presented in Fig. 2 is derived from the initial phase of our interrogation of the OER at oxidised Ni electrodes, yet it illustrates many of the important aspects of the system. To investigate the stability of a Ni anode with respect to oxygen evolution, a freshly prepared electrode was subjected to a series of OER polarisation experiments, one per day, on successive days, in various NaOH electrolytes (1.0–5.0 M). Prior to each experiment, a mild electrochemical pre-treatment was performed by applying a potential cycle to the electrode in 1.0 M NaOH solution. The voltammetric profiles of some of these cycles are presented in Fig. 2a. The steady state polarisation traces of Fig. 2b were recorded in 1.0 M NaOH directly after performing the corresponding cycle from Fig. 2a.

The CVs of Fig. 2a show that the rising edge of significant oxygen evolution current occurs at potentials directly above the peak associated with the Ni(II) → Ni(III) redox transition of the passive oxide film. Some knowledge of this redox process is therefore necessary in understanding the OER at an oxidised Ni surface, although a detailed discussion of the $Ni(OH)_2$/NiOOH transition is beyond the scope of the present article (interested readers are referred to Refs. [44–47]). It should however be noted that an important advance in the understanding of the system was the proposal by Bode et al. [48], of the existence of two coexisting limiting discharged phases, α-$Ni(OH)_2$ and β-$Ni(OH)_2$, and two limiting

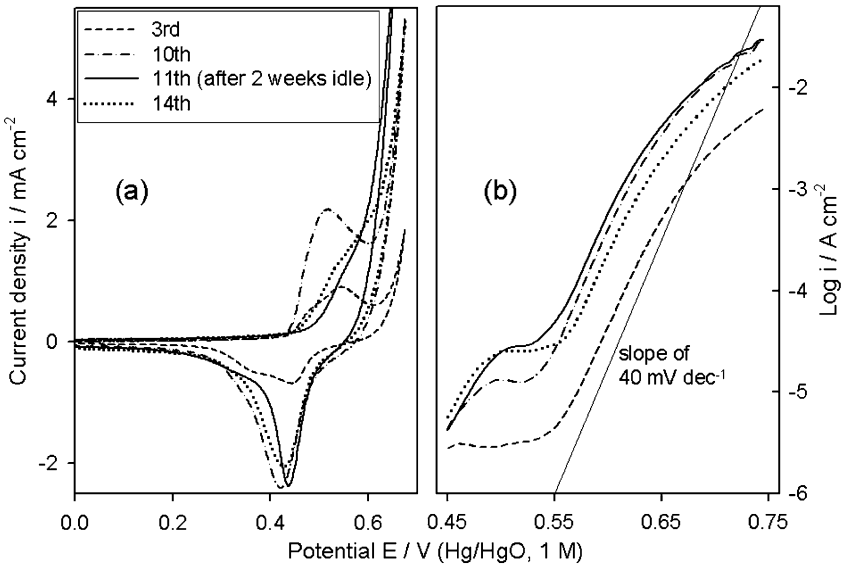

Fig. 2. (a) Pre-treatment CVs recorded in 1.0 M NaOH for a freshly polished Ni electrode (lower and starting limit: −0.8 V, upper reversal potential: 0.675 V, sweep rate: 40 mV s^{-1}). (b) OER steady state polarisation curves recorded in 1.0 M NaOH directly subsequent to the performance of the corresponding pre-treatment potential cycle of Fig. 2a. The legend refers to the number of each experiment (i.e. voltammetric cycle and subsequent polarisation measurement) after the initial performance of such an experiment on the Ni anode when it was freshly prepared.

charged phases, γ-Ni(III/IV) and β-NiOOH. The α-$Ni(OH)_2$ phase (oxidation state 2.0–2.2) is significantly hydrated and disorganised, and upon increasing the electrode potential is oxidised to the non-stoichiometric γ phase (oxidation state 3.5–3.67). The β-$Ni(OH)_2$ phase (oxidation state 2.0–2.2) is largely anhydrous and crystalline and is oxidised to β-NiOOH (oxidation state 2.7–3.0). With a nickel hydroxide sample, we can therefore think of a certain proportion existing in the α–γ "Bode cycle" and the remainder existing in the β–β "Bode cycle". It should however be noted that upon ageing α-$Ni(OH)_2$ can become dehydrated and recrystallise as β-$Ni(OH)_2$, while β-NiOOH can be converted to the γ phase by so-called *overcharge* at extreme anodic potentials. Furthermore, in voltammetric studies, Barnard et al. [49,50] observed that both the oxidation and reduction peaks for material in the α–γ cycle occur at somewhat lower potentials than is the case for the β–β cycle.

Comparing the log $i(E)$ characteristics for the third and tenth polarisation experiments of Fig. 2b, it is apparent that the OER performance of the Ni anode has improved with utilisation (i.e. with electrochemical ageing). The likely explanation can be discerned from the pre-treatment CVs of Fig. 2a, which also serve to characterise the Ni(II)/Ni(III) surface electrochemistry prior to the relevant steady state polarisation measurement. A standard assumption [31,45] when working with electro-generated oxides on Ni anodes, is that there is a direct proportionality between the amount of active material partaking in the Ni(II)/Ni(III) redox transition, and the charge capacity, Q, calculated by integrating the cathodic voltammetric sweep between its uppermost limit and ca. 0 V. Performing such an analysis on the data of Fig. 2a it is found that $Q_{3rd} = \sim 2.8$ mC cm^{-2} compared to $Q_{10th} = \sim 7.9$ mC cm^{-2}. Therefore the superior OER performance of the anode in the tenth experiment can be associated with the presence of a larger amount of the catalytic oxide relative to the fresher electrode. Such behaviour has been previously noted for this system by Gennero De Chialvo and Chialvo [31], who proposed that for nickel oxides of the *same composition* (i.e. either α-$Ni(OH)_2$ or β-$Ni(OH)_2$), the effect is due to an increase in surface roughness with an increasing amount of active oxide. Incidentally, the fact that the amount of active material increased with utilisation despite the fact that the electrode was polished to an apparently bright finish prior and subsequent to each experiment indicates the build-up of a residual oxide, resistant to removal by mechanical polishing. Such behaviour is also observed with iron and cobalt electrodes and we have discussed the "residual oxide" concept elsewhere [38] in relation to the ageing of iron electrodes in alkaline media.

The correlation between redox charge capacity and OER performance appears to falter when we observe enhanced catalytic activity in the eleventh polarisation experiment (Fig. 2b) compared to the tenth, despite the fact that Q_{11th} (= ∼6.6 mC cm^{-2}) is somewhat smaller than Q_{10th}. Note however, that the profile of the 11th voltammogram is significantly different to that of the 10th, with the peak potentials in both the cathodic and anodic directions (if this is meaningful in the latter case) shifted to more positive values. In view of the work of Bernard et al. [49,50], such a shift indicates the existence of a relatively higher proportion of the oxide in the β–β cycle in the 11th experiment compared with the 10th. During the 2 week period between these experiments, the electrode was stored in dry conditions at room temperature, and it is not unreasonable to suggest, in accordance with the Bode scheme [48], that some proportion of the α-$Ni(OH)_2$ has dehydrated to the β phase. This would also account for the superior OER activity noted in the 11th experiment, since it has long been proposed [27] that the charged β phase, β-NiOOH, is the "right type of oxide" for oxygen evolution catalysis. Further electrode use subsequent to the eleventh experiment, sees a decrease in catalytic efficiency – see Fig. 2b, 14th experiment. The corresponding CV in Fig. 2a shows a shift in peak potentials back towards the negative direction, indicative of a reversion of some of the oxide to the α–γ cycle. This is not unexpected, since, as envisaged by Bode et al. [48], β-NiOOH is converted to the γ phase by overcharging at high anodic potentials.

Regardless of catalytic performance, a Tafel slope of $b = \sim 40$ mV dec^{-1} is observed from each of the polarisation curves of Fig. 2b, indicating that the OER mechanism remains invariant with the composition of the oxyhydroxide phase. The irreproducibility in the value of i for a given applied potential, E, which is a feature of Fig. 2b, poses a problem with regard to the determination of the reaction order parameter, $m_{OH^-} = (\partial \log i / \partial \log a_{OH^-})_E$. This was solved by introducing a more rigorous pre-treatment

involving the *pre-reduction* of the Ni electrode for 5 min in 1.0 M NaOH, prior to the application of the potential cycle as previously described. Adopting this approach, acceptable reproducibility was achieved in subsequent polarisation experiments, enabling log $i(E)$ characteristics to be recorded consistently over a range of electrolyte concentrations – Fig. 3. Reaction order plots were constructed from these polarisation curves for various potentials within the ~40 mV dec^{-1} Tafel region. In each case m_{OH^-} was found to be approximately unity – as an example the plot constructed for E = 0.59 V is included as an inset in Fig. 3.

3.2. Cobalt: voltammetry and steady state polarisation

As highlighted for nickel in Section 3.1, a proper understanding of oxygen evolution at a particular oxide electrode, is contingent on having some knowledge about the surface electrochemistry. Accordingly, we introduce the CVs of Fig. 4 at this stage, because we believe that they illustrate an important point regarding the initial passivation of Co electrodes, which in turn will be shown to have an impact on the measured values of the OER kinetic parameters.

The CVs of Fig. 4a are similar to those previously presented by ourselves [33] and other workers [51–56] who have studied this system. The general consensus is that passivation of metallic Co begins with the formation of a Co(II) based oxide film consisting of species such as $Co(OH)_2$ or CoO (peak A II). At higher potentials (peaks A III and A IV) the outer regions of this film are oxidised to a hydrous and dispersed Co(III) based oxide phase. The passive film at anodic potentials is therefore though to exist as a "dual layer" or "sandwich" structure [53], a concept that has been supported by ellipsometry [57,58] and XPS [59] measurements. Peak A V is attributed [5,53,55,56] to the oxidation of the outer region of the Co(III) based oxide to Co(IV) species, with Mössbauer spectroscopy results [60] apparently backing up this viewpoint. Although not apparent from Fig. 4, significant oxygen evolution current appears at potentials immediately positive to peak A V (a CV which illustrates this is included as supplementary data). It is therefore likely that the active catalytic centres for oxygen evolution are Co ions in the +4 valence state, a conclusion that has also been reached for spinel cobaltite phases by several workers [9,10,61].

Comparing Fig. 4a (3.0 M NaOH) with 4(b) (0.5 M NaOH), differences are obvious in the development, with cycling, of the A II peak. For the more concentrated electrolyte, the marked decrease

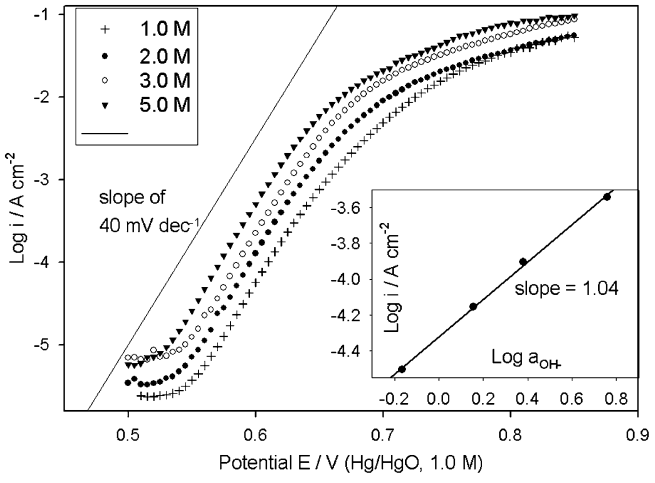

Fig. 3. OER steady state polarisation curves recorded for a pre-reduced Ni electrode in various NaOH solutions. Inset – reaction order plot constructed from the polarisation data at a potential of E = 0.59 V.

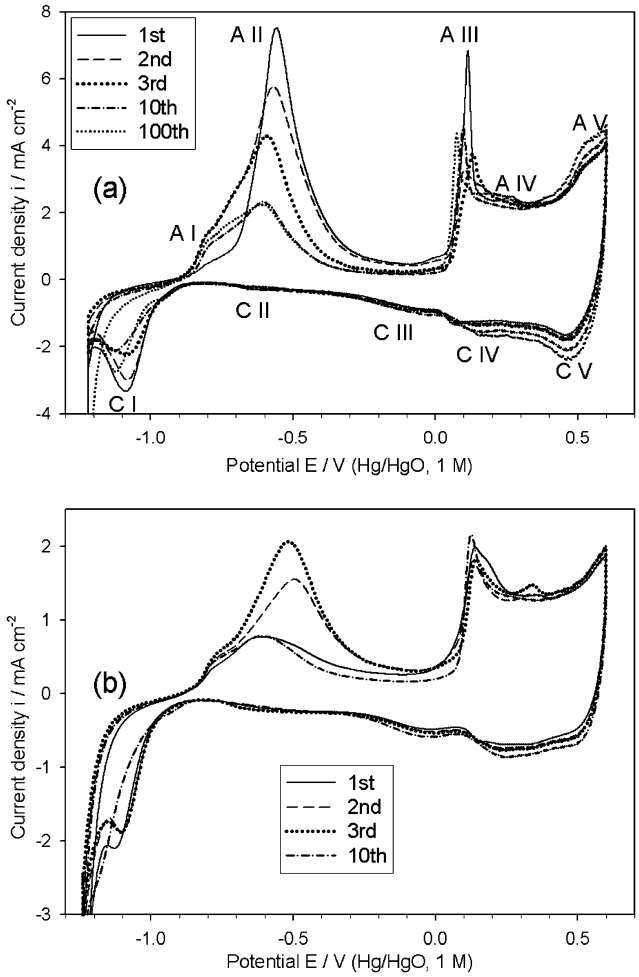

Fig. 4. Potential multi-cycling experiments performed on an initially bright Co electrode in (a) 3.0 M and (b) 0.5 M NaOH solutions. Depicted are analytical CVs recorded between an initial potential of −1.22 V and a reversal potential of 0.6 V at a sweep rate of 40 mV s^{-1}. The intervening cycles were conducted between the same potential limits but at a more rapid scan rate of 300 mV s^{-1}.

over the first few cycles in the charge capacity of this peak, is believed [33,51,52,54] to be related to Co dissolution occurring simultaneously to passive film formation. Based on a combination of rotating ring disc electrode (RRDE) and scanning electrochemical microscopy (SECM) measurements, Erts et al. [62] proposed that the initial passivation of Co in this region of potential (1 M NaOH) occurs via *a rapid dissolution/precipitation* mechanism. However, the developing anodic oxide soon stabilises the system with respect to dissolution – note the similarity in the A II profiles for the 10th and 100th cycles. By contrast, for the more dilute electrolyte (Fig. 4b), the redox capacity of the A II feature actually increases over the first number of cycles. This suggests oxide accumulation primarily by a *solid-state electrochemical* mechanism. Therefore we propose that the initial passivation of Co in alkaline solution evolves from a solid-state reaction to a dissolution/precipitation process, as the OH^- ion concentration is increased. The results of potential cycling experiments, similar to those of Fig. 4 over a range of electrolyte concentrations from 0.25 M $\leqslant$ [OH^-] $\leqslant$ 5.0 M, are included as supplementary data and confirm the aforementioned trend. In addition it is worth noting that Erts et al. [62] detected no soluble species using either RRDE or SECM, when they studied Co in 0.1 M NaOH solution.

In contrast to Ni, it was possible to record reproducible log $i(E)$ plots for the OER at Co anodes, that had received no pre-treatment

beyond polishing. Such plots are presented for several electrolyte concentrations in Fig. 5. It is immediately obvious that there is a difficulty regarding the extraction of the reaction order from this data, namely, the fact that the Tafel slope increases from 38 mV dec^{-1} in 1.0 M NaOH to 46 mV dec^{-1} in 5 M solution. Formally, this implies a change in either OER mechanism or in the rate determining step (RDS) within a given pathway, thus rendering as meaningless any derived value of m_{OH^-}. This difficulty was overcome by subjecting the Co electrode to a pre-treatment involving a 5 min cathodic reduction at −1.15 V in 1 M NaOH, followed by a single potential cycle at 40 mV s^{-1} between −1.22 and 0.6 V in the same solution. Steady state polarisation curves for various NaOH test solutions, recorded subsequent to such pre-treatment, are presented in Fig. 6. With the observation of Tafel slopes of ~46 mV dec^{-1} across the examined range of electrolyte concentration, reaction order plots were constructed for several of the associated values of potential. Typical of these, is the plot for E = 0.6 V, which is included as an inset in Fig. 6 and indicates an m_{OH^-} value of the order of unity.

With repeated use, a gradual increase in Tafel slope was noted for Co electrodes after ca. 20 OER polarisation experiments. A new limiting reproducible log $i(E)$ behaviour became established after ca. 40 experiments, as depicted in Fig. 7. The observation for this "aged" Co anode, of a Tafel slope of ~60 mV dec^{-1} with an associated reaction order approaching 3/2, in tandem with an upper slope of ~120 mV dec^{-1} with $m_{OH^-} = 1$, is strongly reminiscent of OER polarisation data that we have reported elsewhere [37,38] for multi-cycled and "aged" Fe anodes. In Ref. [38] we envisage that this "aged" polarisation behaviour is a product of a particularly inhomogeneous catalytic surface which arises from the build-up of "residual oxide", which we also mentioned in Section 3.1. This viewpoint is supported by a comparison of CVs for freshly prepared and "aged" Co electrodes, which has been included as supplementary data.

3.3. Iron: voltammetry and steady state polarisation

Cyclic Voltammograms recorded in 1.0 M NaOH at various points in the service life of an iron electrode are presented in Fig. 8. We have recently produced a detailed account of the passivation of Fe in alkaline solution [38] and thus offer only a brief outline here. The process begins with the adsorption of OH^- ions at peak A I, followed by the formation of a thin Fe(II) oxide (FeO) or hydroxide ($Fe(OH)_2$) film at peak A II. Only peak A III and its catho-

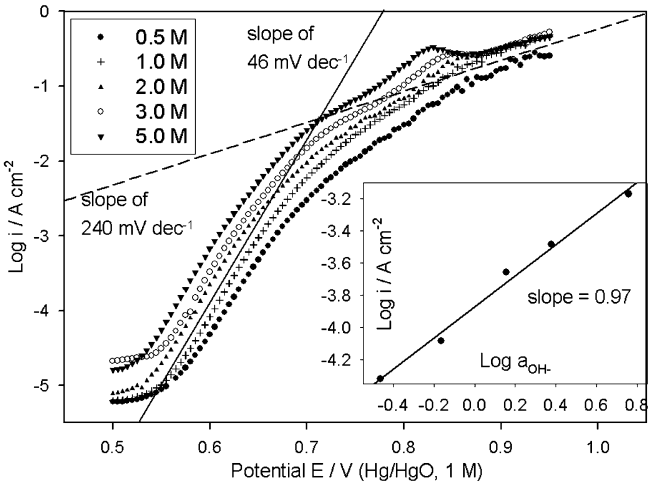

Fig. 6. OER steady state polarisation curves recorded for a pre-reduced Co electrode in various NaOH solutions. Inset – reaction order plot constructed from the polarisation data at a potential of E = 0.6 V.

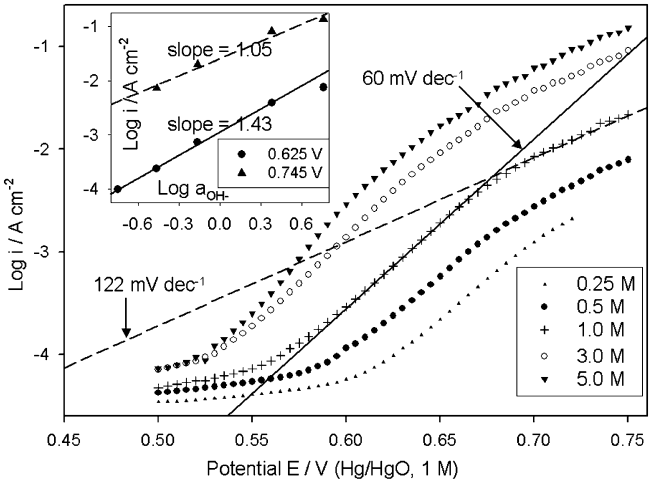

Fig. 7. OER steady state polarisation curves recorded for an "aged" Co electrode in various NaOH solutions. Inset – reaction order plots constructed from the polarisation data at potentials of E = 0.625 V and 0.745 V.

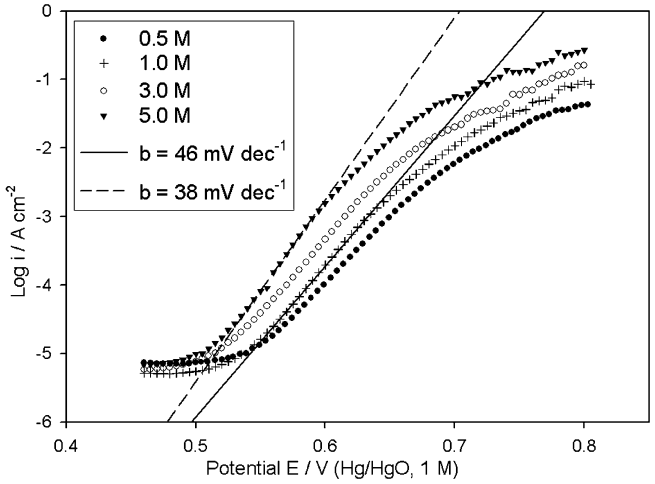

Fig. 5. OER steady state polarisation curves recorded for a brightly polished Co electrode in various NaOH solutions.

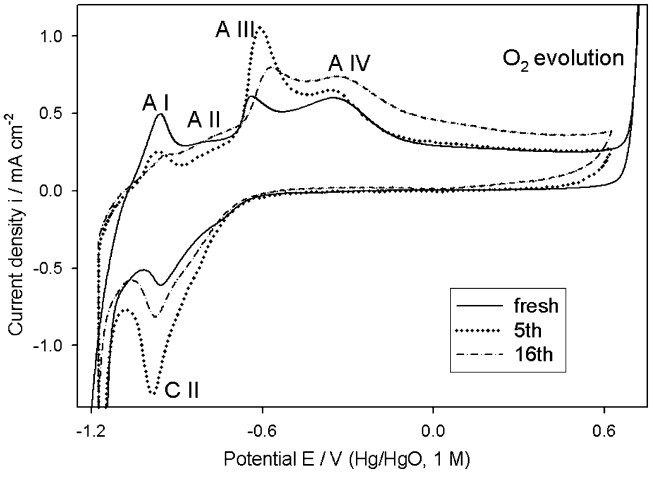

Fig. 8. Cyclic voltammograms (1.0 M NaOH, scan rate = 40 mV s^{-1}) characterising a particular Fe electrode prior to its 1st, 5th and 16th utilisations in OER polarisation experiments.

dic complement C II increase in charge magnitude with repetitive potential cycling [38]. This observation, in tandem with the fact that these peaks exhibit a super-nernstian E-pH dependence of 88 mV/pH unit at 25 °C [63], is suggestive of an Fe(II)/Fe(III) redox transition occurring in an *outer hydrated and dispersed region* of the oxide. We have proposed $[Fe_2O_3(OH)_3(OH_2)_3]^{3-}$ as a formula for the outer Fe(III) based oxide product, with charge neutrality maintained by associated counter-ions [38]. The A IV feature does not exhibit a super-nernstian shift [63] and is therefore attributed to the formation of Fe(III) species (possibilities include Fe_2O_3, FeOOH and Fe_3O_4) in an inner, anhydrous, compact region of the passive film. In contrast to the situation for Ni and Co anodes, there is no obvious oxidation peak at potentials immediately below the onset of the O_2 evolution current in CVs of Fe electrodes – e.g. see the "fresh" profile of Fig. 8. This poses a problem regarding the identity of the valence state of the active sites for the OER. We have considered this problem elsewhere [38] and, based on limited available spectroscopic evidence [64] and thermodynamic data, have concluded that the OER catalytic centres are most likely Fe(VI) based entities.

Amongst the three metals, it proved most difficult to obtain reproducible OER polarisation data for oxidised Fe electrodes. In the absence of electrochemical pre-treatment, a straight-line region with a Tafel slope of ~ 39 mV dec^{-1} was noted in 1.0 M NaOH – however the current at a given potential varied considerably over several repetitions of the experiment. A pre-treatment regime was devised, involving a cathodic reduction at –1.1 V for 5 min in 1.0 M NaOH followed by a single potentiodynamic cycle ($-1.175 \rightarrow 0.625$ V at 40 mV s^{-1}) in the same solution. The CV denoted as "5th" in Fig. 8 was recorded as part of the first application of this regime to a particular anode (four previous non-pre-treated OER polarisation experiments had been conducted). The log $i(E)$ trace labelled as "fresher 1.0 M" in Fig. 9 was measured subsequently and exhibits a Tafel slope of $b = 39$ mV dec^{-1} over the approximate range of $0.65 \leqslant E \leqslant 0.75$ V.

However, even with application of the pre-treatment this result was not entirely reproducible, with incremental increases of 1–2 mV dec^{-1} noted in the Tafel slope in each of the next 4–5 experiments. After this, satisfactory stability was established, with Tafel slope values in the range of 45–48 mV dec^{-1} observed over the course of 15 polarisation measurements in various NaOH test solutions. A representative set of these are presented in Fig. 9, with a reaction order plot for $E = 0.7$ V included as an inset. Although the slight variation in Tafel slope renders the linearity of the latter less satisfactory than is the case in Fig. 3 (for example), it is can be concluded that a reaction order of approximately unity accompanies a slope of $b \approx 2.303 \times 4RT/5F$ (= 47.3 mV dec^{-1} at 25 °C). These kinetic parameters differ markedly from those we observed [38] at similar overpotentials for multi-cycled, and also aged, Fe electrodes (i.e. $b \approx 60$ mV dec^{-1}, $m_{OH^-} = 3/2$). Finally, note that the CV denoted as "16th" in Fig. 8 was typical of those recorded as the final part of pre-treatment during the stable phase of the present study.

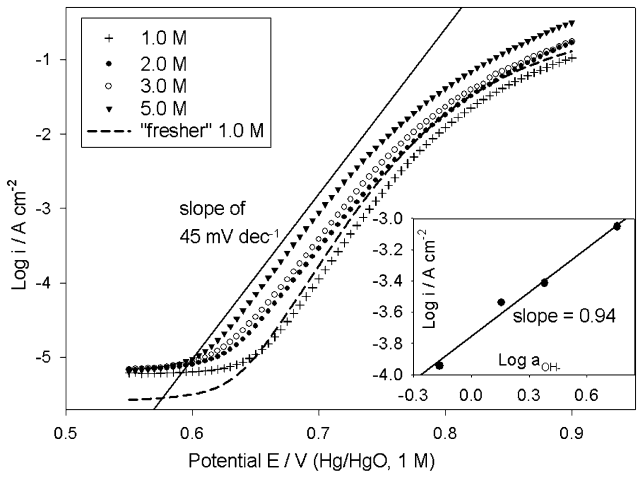

Fig. 9. OER steady state polarisation curves for a pre-reduced Fe electrode in various NaOH solutions. The trace denoted as "fresher 1.0 M" was recorded for the same electrode in an earlier experiment, before satisfactory reproducibility with respect to Tafel slope had become established Inset – reaction order plots constructed from the reproducible polarisation data at a potential of $E = 0.7$ V.

4. Identification of the most likely reaction mechanism

Recapping briefly on the experiment values of the OER kinetic parameters, a lower Tafel slope of $b \approx 2.303 \times 2RT/3F$ (= 39.4 mV dec^{-1} at 25 °C) with $m_{OH^-} = 1$ was observed for electrochemically pre-treated Ni electrodes. By contrast, pre-reduced Co and Fe anodes exhibited $b \approx 2.303 \times 4RT/5F$ with $m_{OH^-} = 1$. Upon ageing, following extensive experimental utilisation, the Tafel slope for Co electrodes increased to $b \approx 2.303 \times RT/F$ (= 59.2 mV dec^{-1} at 25 °C) with a non-integral value of $m_{OH^-} = 3/2$. The latter values of Tafel slope and reaction order had previously been reported for aged Fe anodes [38]. For these aged Co and Fe electrodes, a second Tafel region was resolved at higher overpotentials with $b \approx 2.303 \times 2RT/F$ (= 118.3 mV dec^{-1} at 25 °C) and $m_{OH^-} = 1$. Values of b and m_{OH^-} have not been reported for higher overpotentials in the case of the "fresher" electrodes, owing to unsatisfactory reproducibility. We now address the issue of whether any consistency can be derived from the above results regarding the mechanism of the OER at passivated first row transition metals.

4.1. A pathway for Ni and the importance of the amphoteric nature of the oxide

In a conventional kinetic analysis, a Tafel slope of $2.303 \times 2RT/3F$ is indicative of an RDS subsequent (although not necessarily directly subsequent) to the initial discharge, at each active site, of an OH^- ion from solution. Additionally, if the fractional coverage, θ, of the OER reaction intermediate(s) is assumed to follow the Langmuir isotherm at lower overpotentials (i.e. $\theta \rightarrow 0$), the reaction order of unity suggests that no further hydroxide ions are adsorbed from the bulk electrolyte, prior to, or during, the RDS. From the existing literature, we can identify only two general pathways that satisfy these criteria. The first of these is due to Yeager [65], and takes the form,

$$S^z + OH^- \rightarrow (SOH)^z + e^- \quad (1a)$$

$$(SOH)^z \rightarrow (SOH)^{z+1} + e^- \ldots \text{ RDS}) \quad (1b)$$

$$2(SOH)^{z+1} + 2OH^- \rightarrow 2S^z + O_2 + 2H_2O \quad (1c)$$

where S is an active catalytic site. This scheme encompasses a concept often encountered in the literature, namely, the facilitation of the OER through the cyclic formation and decomposition of an unstable intermediate in a higher valence state ($z + 1$) than the initial state (z) of the transition metal reaction centre. The other possibility, originally proposed for $LaNiO_3$ anodes, is due to Bockris [18]:

$$\{OH^-\}—S^z + OH^- \rightarrow \{OH^-\}—S^z—OH + e^- \quad (2a)$$

$$\{OH^-\}—S^z—OH \rightarrow \text{vac}—S^z—H_2O_2 + e^- \ldots \text{ RDS} \quad (2b)$$

$$(H_2O_2)_{phys} + OH^- \rightarrow (HO_2)^-_{phys} + H_2O \quad (2c)$$

$$(H_2O_2)_{phys} + (HO_2)^-_{phys} \rightarrow OH^- + H_2O + O_2 \quad (2d)$$

$$\{vac\}—S^z + OH^- \rightarrow OH^-—S^z \quad (2e)$$

In scheme (2), {vac} is a vacant oxygen site in the oxide surface, while {OH^-} denotes the occupation of such a site by an OH^- ion. This is a modification of the *physisorbed hydrogen peroxide pathway* (hence the "phys" subscript) proposed, by the same author, for other first row transition metal based perovskites [18]. The {OH^-}—S^z site is formed initially upon the acceptance of a proton by a surface O^{2-} ion from the solvent water. This implies that lattice oxygen atoms participate directly in the gassing reaction, the possibility of which is a subject of literature controversy [66].

For our oxidised Ni anodes, a more satisfactory mechanism can be envisaged, if attention is paid to the underlying surface chemistry. The group of Burke, has reported *negative super-nernstian E*-pH *shifts* for voltammetric peaks associated with hydrous oxide formation for a number of transition metals including Ni [29,45], Fe [63], Au [67], Rh [68] and Ir [69]. Such shifts in peak potential with increasing pH, beyond the expected value of $dE/dpH = -2.303 \times RT/F$ vs. a pH independent reference electrode, imply that the oxidised state has acquired a negative charge relative to the reduced state. This anionic oxide formation arises [70] owing to the well known acidic properties of oxide surfaces in solutions of high pH [71], and can be equivalently regarded [29] in terms of, the adsorption of excess OH^- ions, proton loss from coordinated water molecules or the formation of hydroxyl surface complexes. Although *E*-pH data is not available for oxidised Co electrodes, aspects of the electrocatalytic behaviour of this metal in base are also suggestive of excess OH^- ion coordination at the hydrous oxide surface [54].

In view of the anionic nature of the anodic oxide formed on Rh in base, O'Sullivan and Burke [72] proposed that oxygen evolution on this substrate occurs at surface complexes that can be represented as $[Rh(IV)O_m(OH)_n]^{p-}$, where $p = 2m + n - 4$. Similar considerations should apply to any oxide phase known to acquire a net negative charge in alkaline solution, and therefore we suggest that the active site for the OER on oxidised Ni might be denoted as $[Ni(III)O_m(OH)_n]^{p-}$, where $p = 2m + n - 3$. As in the works of Burke et al. [45,70,72], we emphasise that the formulae for these anionic species are devices presented to rationalise the observed *E*-pH behaviour, where the exact surface stoichiometry is unknown. Indeed, depending on the technique in question, spectroscopic determination of the exact composition and structure of these anionic entities is rendered experimentally challenging by issues such as sample preparation, transfer from solution to vacuum, meaning/reliability of data acquired ex-situ and active gas evolution at the potential of interest during in situ work.

Having considered a reasonable representation of the catalytic surface, we refer next to recent density functional theory (DFT) calculations by Rossmeisl et al. [73,74] in order to obtain some insight into the nature of the OER at such a surface. These calculations indicate that the rate-limiting step is the formation of a superoxy (OOH) species by the addition of an OH^- ion *on top of* an adsorbed oxygen atom. According to this analysis, as electrode potential is raised above the region at which oxygen reduction occurs, the dissociation of OH^- ions on the electrode surface to form adsorbed O atoms is energetically favourable. With increasing potential, the O atom coverage will build-up until it becomes so large, that, at a critical potential, OH adsorption on an already adsorbed oxygen atom is favoured relative to direct coordination with the surface metal cation. Only at this potential (which for all real oxides is significantly larger than the equilibrium potential of the oxygen electrode) will oxygen evolution become possible. In view of these considerations we suggest the following as a feasible pathway for the OER at oxidised Ni in base:

$$[Ni(III)O_m(OH)_n]^{p-} + OH^- \rightarrow [Ni(III)O_{m+1}(OH)_{n-1}]^{p-} + H_2O + e^- \quad (3a)$$

$$[Ni(III)O_{m+1}(OH)_{n-1}]^{p-} \rightarrow [Ni(III)O_m\underline{OOH}(OH)_{n-2}]^{(p-1)-} + e^- \ldots \text{ RDS} \quad (3b)$$

$$[Ni(III)O_m\underline{OOH}(OH)_{n-2}]^{(p-1)-} + 2OH^- \rightarrow [Ni(III)O_mO_2(OH)_{n-1}]^{p-} + H_2O + e^- \quad (3c)$$

$$[Ni(III)O_m\underline{OO}(OH)_{n-1}]^{p-} + OH^- \rightarrow [Ni(III)O_m(OH)_n]^{p-} + O_2 + e^- \quad (3d)$$

For an oxidised metal electrode in aqueous alkaline solution, the quantum chemical analysis of Rossmeisl et al. [73] indicates that the coordination of oxygen atoms by the surface metal ions will increase as electrode potential is raised. This process is facilitated by the progressive oxidation of the metal ion to higher valance states. Of interest to us, is what happens when the metal ion is already in its highest possible valance state – e.g. +3 for Ni. The Ni cation on the left hand side of Eq. (3a) is assumed to have the maximum coordination ($m + n$) permitted by the valance state and the charge $p-$ on the surface complex. It can coordinate a further O atom only by the displacement of an OH species, as in Eq. (3a). The surface cation may now be considered to be saturated with respect to coordination, given its stronger interaction (double bond character) with the O atom in comparison to the OH group (single bond character).

When a further OH^- ion (which may come from the surface complex as in Eq. (3b), or, more generally from solution – see Section 4.2) attempts to dissociate in the vicinity of the saturated cation, it is energetically more favourable for this to proceed atop one of the existing coordinated O atoms, rather than for direct coordination to occur to the metal ion – see rate determining step 3b. It is worth noting that this step involves the weakening of a Ni(III)—O bond from double bond to single bond character. The superoxy species formed in step 3b has been underlined so that its progress through the remainder of the mechanism can be readily tracked.

In contrast to the RDS of scheme 2, the electron passed to the external circuit in step 3b is supplied by a coordinated OH^- ion, bringing a decrease of one in the overall negative charge on the surface complex. Of course the concepts of anionic surface complexes and of hydroxide ions occupying lattice vacancies are essentially just different model approaches to the observed anionic character of hydrous oxides in base. However, the fact that the former dispenses with the need to admit the direct participation of lattice oxygen atoms in the OER, should make this representation more widely acceptable.

To satisfy ourselves that mechanism three is consistent with the experimental kinetic parameters, we briefly outline the formal kinetic mechanistic analysis. The reaction fluxes j (units: mol cm^{-2} s^{-1}) for step (3a) in the forward and reverse directions can be respectively written as:

$$j_a = k_a'^0 a_{OH^-}(1-\theta)\exp(\beta\eta F/RT) \quad (4)$$

$$j_{-a} = k_{-a}'^0 \theta \exp(-(1-\beta)\eta F/RT) \quad (5)$$

In Eqs. (4) and (5), θ is the fractional coverage of the electrode surface by $[Ni(III)O_{m+1}(OH)_{n-1}]^{p-}$, β is the electron transfer symmetry factor, while $k_a'^0$ and $k_{-a}'^0$ are standard electrochemical rate constants. The potential dependence of the reaction rate is considered in terms of the oxygen overpotential η – it is worth noting that at 25 °C the reversible oxygen potential is 0.303 V vs. Hg/HgO in the same solution [34]. It is assumed that (3b) is the RDS – applying the pseudo-equilibrium principle to step (3a) we equate (4) and (5) and solve for θ,

$$\theta = \frac{Ka_{OH}e^{\eta F/RT}}{1 + Ka_{OH}e^{\eta F/RT}} \quad (6)$$

where, $K = k_a'^0/k_{-a}^0 = \exp(-\Delta G'^0/RT)$. At lower values of η, the latter free energy term dominates the exponents in Eq. (6), with the implication that $Ka_{OH}\, e^{\eta F/RT} \ll 1$, which in turn means that Eq. (6) reduces to:

$$\theta = Ka_{OH} \exp(\eta F/RT) \tag{7}$$

Formally, the fact that $\theta = Ka_{OH}\, e^{\eta F/RT} \ll 1$, means that the low coverage Langmuir isotherm is applicable at lower overpotentials. The rate equation for step (3b) is:

$$j_b = k_b'^0 \theta \exp(\beta\eta F/RT) \tag{8}$$

Substituting for θ from Eq. (7), an expression for the overall OER current density, i, can be written by noting that the RDS limits the rate of transfer of two electrons:

$$i = 2Fj_b = 2FKk_b'^0 a_{OH} \exp((1+\beta)\eta F/RT) \tag{9}$$

Performing a logarithmic analysis of Eq. (9), with the assumption of a symmetrical electron transfer energy barrier (i.e. $\beta = ½$), yields $b = 2.303 \times 2RT/3F$ and $m_{OH^-} = 1$, both in accord with the experimental data.

Conventional kinetic analyses of schemes 1 and 2 take the same form as Eqs. (4)–(9) and therefore these pathways cannot be dismissed on the basis of experimental electrochemical kinetic data. For both of these mechanisms, the dioxygen entity that will subsequently be evolved as molecular oxygen is formed by the interaction of an adsorbed OH species with a OH^- ion. However the DFT calculations of Rossmeisl and co-workers [73,74] indicate that the critical dioxygen formation is more likely to occur at an adsorbed O atom than at adsorbed OH. It is on this basis that we suggest that our new mechanism (3) is more appropriate than schemes 1 or 2.

Owing to the extreme irreversibility of the oxygen evolution and reduction processes, it has long been appreciated [75], that the principle of microscopic reversibility is unlikely to apply to the oxygen electrode. As a consequence, steady state kinetic data on the OER can only yield mechanistic information up to and including the RDS. The details of the subsequent steps are therefore inevitably speculative. We propose that, subsequent to the RDS in step 3c, a proton is transferred from the superoxy species to an OH^- ion in solution. The majority of the bonding electron density is then concentrated between the two oxygen atoms, with the result that the dioxygen entity is readily displaced by the adsorption of an OH species in step 3d, leading to molecular oxygen evolution and the restoration of the active site to its original condition (as on the left hand side of step 3a). It can thus be appreciated that oxygen evolution is the mechanism by which a metal oxide surface "copes" with the potential driven dissociation of OH^- ions from solution, where the surface metal cations are already fully coordinated in their highest valance state.

4.2. The dual barrier model and a mechanism for Co and Fe anodes

The Tafel slope of $b \approx 2.303 \times 4RT/5F$ observed for Co and Fe electrodes cannot be rationalised by kinetic analyses of any of the commonly cited OER pathways, regardless of which step is chosen as RDS, or the adsorption isotherm admitted (Langmuir or Temkin) – cf., Ref. [18], Table II. This does not however mean that mechanistic details cannot be derived – it merely implies that a more complicated model of the electrode/solution interface is required. In the present context we refer to a *dual barrier model* developed by MacDonald and Conway [76] to rationalise OER kinetic data obtained for Au electrodes. This model owed much to earlier work by Meyer [77] on cathodic electrode processes.

The model of MacDonald envisages that only a fraction, V_s, of the potential difference, E, between metallic electrode and electrolyte is effective in lowering the potential barrier to interfacial electron transfer. In series with this, the remainder, V_f, appears across an electronically conducting "barrier" oxide, through which the charge passed in the OER must migrate under the influence of an electric field. Where a normal (symmetrical single barrier) kinetic analysis yields $b = 2.303 \times 2RT/3F$ for a particular step of an OER pathway considered to be rate-limiting, the overall rate equation takes the general form (cf., Eq. (9)),

$$i = wi_0 \exp((1+\beta_s)EF/RT) \tag{10}$$

where, i_0 is the exchange current density for the OER, and w is a constant that would equal unity had we chosen to write the equation in terms of η rather than E. On the other hand, if the OER is proceeding in the steady state under dual barrier conditions, its RDS must be in equilibrium with the barrier film charge migration process. Therefore it is possible to obtain an expression for the overall current density across the two barriers by equating Eq. (10) with the rate equation for the oxide charge migration. It can be shown [76,77] that the resulting expression has the form,

$$i = W \exp((1+\beta_t)EF/RT) \tag{11}$$

where

$$\beta_t = \frac{\beta_f \beta_s}{\beta_f + \beta_s} \tag{12}$$

In Eq. (12), β_f is the symmetry factor for field assisted charge transport through the oxide and β_t is therefore a *composite symmetry factor* taking account of the two potential energy barriers. The W factor in Eq. (11) depends on i_0 and also on the exchange current density for the charge migration process, which in turn depend respectively on a_{OH^-} and the activities of the barrier film charge carriers [77]. Neither Meyer [77] nor MacDonald [76] speculated as to the detailed nature of the barrier film charge migration process or indeed as to the exact identity of the charge carriers, since, as will become obvious, these factors are formally unimportant with regard to the identification of the mechanism of the OER at the oxide film/solution interface.

While MacDonald's treatment didn't extend to reaction orders, the analysis of Meyer [77] indicates that, under dual barrier conditions, the measured reaction order with respect to the activity, a_s, of a particular reactant in the electrochemical charge transfer reaction is given by,

$$\left(\frac{\partial \log i}{\partial \log a_s}\right)_E = \frac{m_s \beta_f}{\beta_f + \beta_s} \tag{13}$$

where, m_s, is the value that would be measured for the relevant reaction order under the more usual single (interfacial electron transfer) barrier condition.

If we assume that both potential barriers are symmetrical (i.e. $\beta_f = \beta_s = ½$), Eq. (12) predicts that $\beta_t = ¼$. Under these conditions, a logarithmic analysis of Eq. (11) yields $b = 2.303 \times 4RT/5F$, implying that the OER mechanism we seek is characterised by $b = 2.303 \times 2RT/3F$ under single barrier conditions. Also, referring to Eq. (13), $\beta_f/\beta_f + \beta_s = ½$, which means that the reaction order of approximately unity, measured under dual barrier conditions, corresponds to an expected value of $m_{OH^-} = 2$ in a single barrier treatment of the appropriate pathway. Therefore a suitable OER mechanism for the Co and Fe electrodes must give rise to $b = 2.303 \times 2RT/3F$, $m_{OH^-} = 2$ in a conventional single barrier analysis.

Several commonly cited mechanisms meet these criteria when a particular step is considered to be rate determining under conditions of low coverage ($\theta \to 0$) of intermediates. These include the often proposed Krasil'shchikov path [24], Bockris's electrochemical path [18] and the more general form of the physisorbed peroxide

path [18,38]. It is significant, as discussed elsewhere [38], that amongst these only the latter path can rationalise the experimental values of b and m_{OH^-} observed for "aged" Co (Fig. 7) and Fe [38] anodes. However in Section 4.1, it was commented that the physisorbed peroxide type mechanism seems unlikely in view of the recent analyses of Rossmeisl et al. [73,74]. This implies that a new pathway must be devised to account for the range of experimental kinetic parameters observed for Co and Fe anodes. Following on the discussion of Section 4.1, we propose the following to be a feasible reaction mechanism for the OER at both fresh and aged Fe electrodes:

$$[Fe(VI)O_m(OH)_n]^{p-} + OH^- \rightarrow [Fe(VI)O_{m+1}(OH)_{n-1}]^{p-} + H_2O + e^- \quad (14a)$$

$$[Fe(VI)O_{m+1}(OH_{)n-1}]^{p-} + OH^- \rightarrow [Fe(VI)O_m\underline{OOH}(OH)_{n-1}]^{p-} + e^- \ldots \text{ RDS} \quad (14b)$$

$$[Fe(VI)O_m\underline{OOH}(OH)_{n-1}]^{p-} + OH^- \rightarrow [Fe(VI)O_m\underline{OO}(OH)_{n-1}]^{p-} + H_2O + e^- \quad (14c)$$

$$[Fe(VI)O_m\underline{OO}(OH)_{n-1}]^{p-} + OH^- \rightarrow [Fe(VI)O_m(OH)_n]^{p-} + O_2 + e^- \quad (14d)$$

We retain from Section 4.1 the concept of the catalytically active site existing in the form of an hydroxylated anionic surface complex – for Fe(VI), $p = 2\,m + n - 6$. Indeed, since Fe(VI) species (probably in the form of FeO_4^{2-}) are soluble in aqueous alkaline solution [78], their stabilisation on the oxide surface by the coordination of excess OH^- ions provides a tentative explanation as to how they can act as OER active centres. Pathway 14 is also suitable for Co anodes, except in this case the active site is represented as $[Co(IV)O_m(OH)_n]^{p-}$ ($p = 2\,m + n - 4$), in agreement with the proposal of Gennero De Chialvo and Chialvo [36] that the catalytic species is unlikely to exist as discrete CoO_2 entities.

In the limit of low intermediate species coverage ($\theta \rightarrow 0$), the kinetic analysis of scheme 14 is very similar to that of scheme 3, except that there is an addition factor of a_{OH} in the rate equation for the RDS relative to Eq. (8). This means that while the Tafel slope prediction remains $b = 2.303 \times 2RT/3F$, the anticipated reaction order doubles to $m_{OH^-} = 2$, as required (when correction is made for the dual barrier) to rationalise the data of Figs. 6 and 9. We have described in detail elsewhere [38], how an analysis of the general physisorbed peroxide mechanism yields the values of $b = 2.303 \times RT/F$ and $m_{OH^-} = 3/2$ observed at lower η for aged Fe and Co anodes, if the fractional coverage of the intermediate formed in the initial discharge step is governed by the Temkin adsorption isotherm ($0.2 \leqslant \theta \leqslant 0.8$). It was shown, that to obtain these values of b and m_{OH^-} in kinetic analysis, it is necessary that r_I, the rate of change of the free energy of adsorption with θ of the intermediate formed in the initial step, be significantly greater than the corresponding parameter r_{II} for the intermediate species formed in the subsequent and rate determining step. The applicability of the physisorbed H_2O_2 mechanism to this situation arises from the fact that the OH entity formed in the opening step (cf., Eq. (2a)) is chemisorbed, while the H_2O_2 formed in the second step (cf., Eq. (2b)) is associated to the electrode surface through a weaker interaction. Examination of scheme 14 reveals that similar considerations prevail here – the adsorbed oxygen atom formed in step 14 a is double bonded to the metal cation, whereas the Fe(VI)—OOH bond of step 14 b is of single bond character. Hence, as with the physisorbed peroxide pathway, it can reasonably be assumed that $r_I \gg r_{II}$ for the "superoxy" pathway of Eq. (14). Therefore a conventional analysis of pathway 14 under Temkin conditions will yield the OER kinetic parameters noted for aged Fe and Co electrodes at lower η.

At higher η, the analysis predicts $b = 2.303 \times 2RT/F$ and $m_{OH^-} = 1$, where it is assumed that the intermediate coverage has passed beyond the Temkin potential window and can now be represented as $\theta \rightarrow 1$ [38]. It is of course possible that the different Tafel slopes observed for Co and Fe under different conditions of age and overpotential are indicative of different OER mechanisms, however as discussed for Pt electrodes by Damjanovic et al. [79], changes in intermediate coverage rather than pathway provide a more satisfactory solution for such observed behaviour.

4.3. The nature of the oxide barrier to charge transport

Referring to Fig. 9, why do dual barrier conditions not prevail for the freshest pre-reduced Fe anode ($b = 39$ mV dec^{-1}), when their effect is evident on the kinetic parameters (b increases to ca. 45 mV dec^{-1}) observed for the more utilised electrode? We believe that the key to answering this question lies in the respective pretreatment CVs of Fig. 8 – recall that the CV entitled "5th" was recorded prior to the 39 mV dec^{-1} log $i(E)$ plot, while that denoted as "16th" was typical of those recorded prior to the measurement of Tafel lines with $45 \leqslant b \leqslant 48$ mV dec^{-1}. It is noteworthy that the redox charge capacity of the A III/C II peak pair, which is associated with the outer hydrous region of the oxide (recall Section 3.3), is greatly enhanced in the "5th" CV relative to the "16th". By contrast the A IV peak is more significant in the "16th" CV, implying that, with repeated utilisation, the inner compact region develops a greater relative influence on the overall properties of the passive film. This observation suggests an identification of the film charge transport barrier with the anhydrous inner oxide or with the interface between this region and more dispersed hydrous outer oxide. The duplex layer model for anodic oxides developed by Burke and co-workers [69,80,81], envisages that the ions of the inner region are held in place by a rigid network of polar covalent bonds, through which ionic transport is difficult, thus limiting growth to perhaps no more than five monolayers. It is significant that this description fits the profile of a "barrier oxide" as outlined by Meyer [77] and MacDonald [76]. On the other hand, charge percolation proceeds comparatively easily and quickly through the outer, hydrous, polymeric oxide region – e.g. we have recently calculated [38] that the average rate of charge diffusion for a hydrous oxide covered Fe electrode in base is comparable to that of electrodes modified by redox polymers such as poly(pyrrole). Interestingly, a duplex model was also specifically proposed [82] for the anodic oxide formed on Au electrodes – the very system for which the twin barrier model was originally applied to the OER [76].

The association of the charge transport barrier with the inner layer of the passive film also provides a satisfactory explanation for the decreasing applicability of the dual barrier model with increasing test solution concentration for non-electrochemically pre-treated Co electrodes (Fig. 5). As discussed in Section 3.2, a rapid dissolution/precipitation mechanism becomes increasingly important in the initial passivation of bright Co, as the OH^- concentration of the electrolyte is raised above 1.0 M. For more dilute alkaline solutions, solid-state electrochemical oxidation of the metal, with the initial formation of a compact oxide phase (as proposed by the duplex layer model), is of primary importance. This explains the dual barrier Tafel slope behaviour observed for 1.0 M NaOH in Fig. 5. The oxide formed in more concentrated alkaline electrolyte where dissolution/precipitation predominates, is expected to be somewhat crystalline, with a high defect density due to the rapid rate of re-precipitation. This phase should be characterised by a higher ionic mobility, and thus present a significantly reduced potential barrier to charge migration. Accordingly, the log $i(E)$ plot recorded in 5.0 M NaOH for an initially bright Co electrode exhibits a Tafel slope of 38 mV dec^{-1}, characteristic of just the conventional potential barrier to interfacial electrochemical charge transfer. This interpretation is supported by the data of Fig. 6, where for each experiment, initial passivation of the elec-

trode following polishing and pre-reduction took place in 1.0 M NaOH. Dual barrier Tafel behaviour was then noted in subsequent OER steady state polarisation measurements, regardless of the concentration of the test solution. It should also be noted that there is some evidence in Fig. 6. of a second Tafel region at higher η, with a very high slope of the order of 240 mV dec^{-1}. As discussed by MacDonald [76], such a slope ($b \approx 2.303 \times 4RT/F$) is also consistent with the twin barrier model.

5. Estimation of electrode roughness factors

An appraisal of 15 of the most common techniques for electrode real surface area determination has been provided by IUPAC [83] – however amongst those considered, not one is particularly suitable for the case of anodic oxide covered non-precious metals. Even though we have performed impedance spectroscopy measurements on the electrodes considered here, significant frequency dispersion was noted in each case for the double layer capacitance [40], thereby casting significant doubt over roughness factors calculated by the capacitance ratio approach.

In view of this, the most appropriate method that could be identified was the OH_{ads} desorption technique of Ho and Piron [42,43], the measurement principles of which, have already been detailed in Section 2. A Q_{dec} vs. E plot (as defined in Section 2) for a freshly prepared, non-pre-reduced Ni anode in 1.0 M NaOH is presented in Fig. 10, along with the associated OER steady state polarisation plot. Similar data for fresh Co and Fe electrodes are included as supplementary information. Following the interruption of anodic charging at an OER steady state current density of i_{appl}, self discharge of the electrode occurs through the decomposition of the electrosorbed oxygen evolution intermediate species. As pointed out by Conway and Bourgault [84] the discharge process continues until the metal ions of the oxide surface have returned to the valence state that is stable at the reversible oxygen potential (i.e. 0.303 V vs. Hg/HgO in the same solution at 25 °C – recall Section 4.1). Noting from pathways (3) and (14) that the only intermediates to achieve significant fractional coverage will be those formed in the initial step of the respective mechanisms, and examining the potentials of the various redox peaks in the CVs of Figs. 2, 4 and 8, we propose that the experimentally observed cathodic discharge currents arise due to the following reactions for Ni, Co and Fe respectively.

$$[Ni(III)O_{m+1}(OH)_{n-1}]^{p-} + H_2O + 2e^- \rightarrow [Ni(II)O_m(OH)_n]^{p-} + OH^- \quad (15)$$

$$[Co(IV)O_{m+1}(OH)_{n-1}]^{p-} + H_2O + 2e^- \rightarrow [Co(III)O_m(OH)_n]^{p-} + OH^- \quad (16)$$

$$[Fe(VI)O_{m+1}(OH)_{n-1}]^{p-} + H_2O + 4e^- \rightarrow [Fe(III)O_m(OH)_n]^{p-} + OH^- \quad (17)$$

Plateau regions of approximately constant Q_{dec} are evident in our Q_{dec} vs. E plots (e.g. Fig. 10) at potentials above the lower straight-line Tafel regions of the associated log i vs. E plots. It was envisaged by Ho and Piron [43] that such plateaus correspond to desorption of the reaction intermediate for the situation where $\theta \rightarrow 1$. Furthermore, after Fedorova and Frumkin [85], they assumed that the charge passed per real cm^3 of surface area during a two electron desorption (as in Eqs. (16) and (17)) of a monolayer of intermediate species could be taken as 420 μC cm^{-2}. For Ni and Co, the roughness factor, f_r, relevant to the OER can thus be *estimated* as follows:

$$f_r = \frac{Q_{dec}(\text{plateau})}{420 \mu C\,cm^{-2}} \quad (18)$$

It is emphasised that f_r, as calculated by this method is just an estimate – the approach is based upon a number of assumptions, foremost amongst which is the benchmark value of 420 μC cm^{-2}, described by Ho and Piron [43] as being merely a reasonable "accepted standard". However we seek, not to establish absolute values of true surface area, but rather to obtain consistent roughness factor estimates, to facilitate a meaningful comparison of the intrinsic activities of the passive oxides of the three metals for the OER. The desorption is envisaged (Eq. (17)) to involve a four electron discharge in the case of Fe electrodes – the denominator of Eq. (18) must therefore be doubled to 840 μC cm^{-2} for this system.

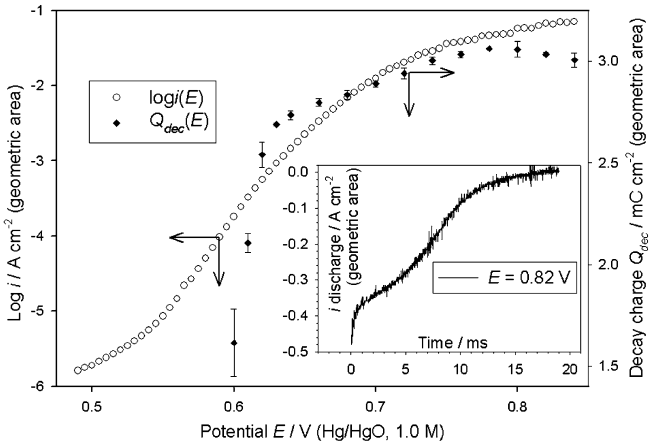

Fig. 10. The cathodic charge Q_{dec} passed during the discharge of a freshly prepared Ni electrode in 1.0 M NaOH plotted against the potential E that corresponds to the prior anodic charging current density i_{appl}. The relationship between i_{appl} and E is derived from the OER steady state polarisation plot (log i vs. E) for the same system (also shown). Inset – an example of one of the discharge transients for a value of i_{appl} corresponding to E = 0.82 V.

Referring to the plateau region of Fig. 10 (0.76–0.82 V), a reasonable value of Q_{dec} (plateau) is 3.05 ± 0.05 mC cm^{-2}, which leads to f_r = 7.3 ± 0.1. Similar measurements on freshly prepared, non-pre-reduced Co and Fe electrodes in 1.0 M NaOH yielded respectively f_r = 13.1 ± 0.5 and f_r = 0.52 ± 0.02. The sub-unity roughness factor estimated for Fe is not surprising, given the model we outlined in Section 4.2 for the active surface in this case – i.e. the stabilisation of some Fe(VI) centres against dissolution by the coordination of excess OH^- ions to form the catalytic $[Fe(VI)O_m(OH)_n]^{p-}$ entity.

6. The activity series of the passive oxides of Fe, Co and Ni for the OER

OER polarisation plots, normalised to the active surface area based on the f_r estimates of the previous section, are presented in Fig. 11 for freshly prepared non-pre-reduced Ni, Co and Fe anodes in 1.0 M NaOH. In accordance with the comments of Bockris [86,87], the relative activities of the three electrodes for the OER are compared in terms of the real current density at a potential in the practically important lower Tafel region, rather than on the basis of i_0 values – see Table 1. The values of $i_{(E=0.605V)}$ suggest that catalytic performance decreases in the order Ni > Co > Fe. Caution is however required in that there is a greater electrical contribution to the current density at a given potential for the Ni and Fe electrodes owing to the higher transfer coefficient of $\alpha \approx 3/2$ for these systems, compared to the value of $\alpha \approx 5/4$ that prevails for Co – recall that $i(\eta) = i_0 \exp[\alpha\eta F/RT]$. This arises due to the overpotential 'lost' to the oxide charge migration process (dual barrier model) for Co, and the situation is further complicated by the fact that where dual barrier conditions apply, the equilibrium potential is a mixed potential and not simply the reversible oxygen potential. We can only comment that, at the onset potential of the Tafel

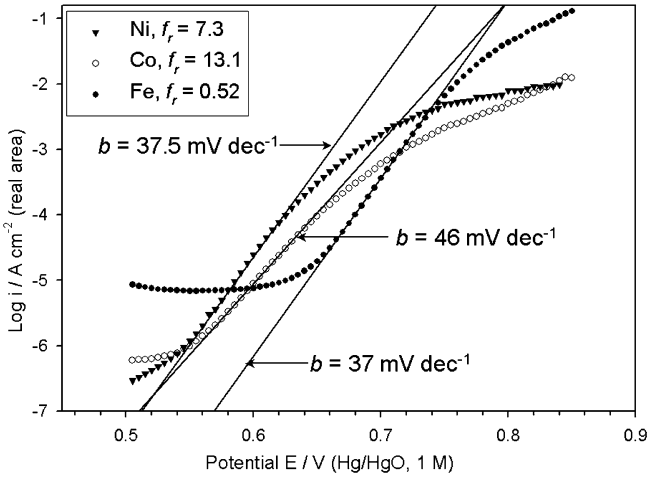

Fig. 11. Comparison of OER steady state polarisation curves, normalised to the estimated active surface area, for freshly prepared, non-pre-reduced Ni, Co and Fe electrodes in 1.0 M NaOH.

Table 1
Various OER electrocatalytic parameters extracted from the data of Fig. 11.

Electrode	f_r	b/mV dec^{-1}	$i_{(E=0.605V)}$/A cm^{-3}
Ni	7.3 ± 0.1	37.5	$3.34(\pm0.05) \times 10^{-5}$
Co	13.1 ± 0.5	46.0	$1.15(\pm0.04) \times 10^{-5}$
Fe	0.52 ± 0.02	37.0	$9.5(\pm0.4) \times 10^{-7}$[a]

[a] Estimated by extrapolation of the lower Tafel slope.

region for the Co anode (ca. 0.56 V), it exhibits a lower rate of oxygen evolution than does Ni – if the effect of the charge migration barrier could be factored out by extending a $b = 2.303 \times 2RT/3F$ Tafel line through this point, Co would still display a lower catalytic activity than Ni at $E = 0.605$ V.

The apparent activity trend outlined above is in agreement with results obtained by Bockris and Otagawa [86] for the OER at various perovskite electrodes in 1.0 M NaOH at 25 °C. Specifically, these workers quoted the following real current densities at $\eta = 0.3$ V (i.e. $E = 0.603$ V): $i = 1.3 \times 10^{-5}$ A cm^{-2} for a nickelate anode ($f_r = 5.6 \times 10^3$), $i = 1.4 \times 10^{-6}$–1.0×10^{-5} A cm^{-2} for various cobaltate anodes (f_r values of the order of 10^2–10^3), $i = 5.0 \times 10^{-7}$ A cm^{-2} for a $La_{0.7}Sr_{0.3}FeO_3$ anode ($f_r = 6.0 \times 10^2$) and $i = 8.1 \times 10^{-7}$ A cm^{-2} for a $La_{0.5}Sr_{0.5}FeO_3$ anode ($f_r = 3.3 \times 10^3$). Comparing these values to those of Table 1, order of magnitude agreement is evident between the values quoted for our electrodes and the perovskite electrodes (based on the corresponding transition metal), despite the fact that the latter exhibit much larger roughness factors. It is therefore interesting to note that when correction is made for active surface area, the passive oxides exhibit similar intrinsic catalytic activities for the OER compared to the corresponding perovskite phases, despite the structural differences between these classes of oxides.

In an effort to formulate a coherent theory of electrocatalysis for the OER, Bockris and Otagawa [86] noted that, while calculated values for the M(III)—OH (M is a first row transition metal) bond strength decreased on traversing the periodic table from V to Ni, the value of $i_{\eta=0.3V}$ exhibited the opposite trend for perovskites based on these metals. Consistent with their proposal of the physisorbed hydrogen peroxide path (cf., scheme 2, Section 4.1) as the operative mechanism for oxygen evolution at perovskite surfaces, the aforementioned trends were rationalised in terms of an RDS involving desorption of an adsorbed OH species. These workers then constructed molecular orbital diagrams for the bonding of an OH entity to $M(III)O_5$ and showed, on this basis, that M—OH bond strength is inversely proportional to the number of d electrons occupying antibonding orbitals (4 for Ni(III)—OH, 3 for Co(III)—OH, etc.). In this way OER activity was correlated to the total number of d electrons in the metal ion of the catalytic site.

By contrast Rossmeisl et al. [73,74] have devised a volcano plot in which oxygen evolution activity is correlated to the binding energy of O to the electrode surface. Since our proposed pathway (schemes 3 or 14) involves, as its RDS, the weakening of a metal cation – oxygen double bond to a single bond, it is to be expected that the metal ion with the strongest oxygen bond will exhibit the poorest OER catalytic performance. However since M—O bond strength is also likely to exhibit dependence on the number of d electrons, the same trends are expected whether one chooses M—O or M—OH bond strength as the descriptor of catalytic activity. Therefore, our observation of the same activity series as Bockris and Otagawa (albeit for a more limited range of elements), despite the fact that we envisage the rate-limiting process to involve the weakening of M=O as opposed to the desorption of OH, would seem to verify the aforementioned theory of those authors with respect to the significance of antibonding d electrons. It is worth remembering however, that we envisage for Ni, Co and Fe respectively, that M(III), M(IV) and M(VI) to oxygen bonds are weakened in the RDS. This contrasts with the simple MO_5—OH molecular orbital picture of Bockris and Otagawa [86], which assumes (with rather little experimental evidence) an M(III) active site regardless of the identity of M. It is likely that the Bockris antibonding d electron, electrocatalytic theory is correct in essence, but it may be oversimplified in its assumption of a common valence state, across the periodic table, for the active metal ion.

7. Conclusions

An OER reaction pathway, involving the formation of an —OOH intermediate as its rate-limiting step, has been found to be most suitable in the rationalisation of the various experimental kinetic parameters observed for passive oxide covered Co and Fe anodes. A similar, though not identical, mechanism is likely for oxidised Ni. Amongst the three oxides, the latter is the most efficient OER electrocatalyst, with Fe electrodes displaying the poorest performance. Given the nature of the envisaged mechanism, this activity series is consistent with the theory of OER electrocatalysis proposed by Bockris, which emphasises the importance of the number of d electrons in the metal cation.

Knowledge of the chemical and structural properties of the underlying oxide phase is significantly useful in understanding the OER. For example, the amphoteric character of the hydrous anodic oxides implies that it is more realistic to view the OER active sites in terms of anionic surface complexes rather than the traditional viewpoint of stoichiometric units of the bulk oxide – e.g. $[Ni(III)O_m(OH)_n]^{p-}$ ($p = 2m + n - 3$) in preference to Ni(III)OOH. Furthermore, it has been demonstrated that an oxide charge migration barrier, which in some circumstances affects the experimental values of the OER Tafel slope, can be identified with the inner compact anhydrous region of the passive oxide films of Co and Fe.

Appendix A. Supplementary material

Supplementary data associated with this article can be found, in the online version, at doi:10.1016/j.jelechem.2009.11.024.

References

[1] D.E. Hall, J. Electrochem. Soc. 130 (1983) 317–321.
[2] K. Kinoshita, Electrochemical Oxygen Technology, Wiley-Interscience, New York, 1992.

[3] A.C.C. Tseung, S. Jasem, Electrochim. Acta 22 (1977) 31–34.
[4] S.I. Cordoba, R.E. Carbonio, M. Loprz Teijelo, V.A. Macagno, Electrochim. Acta 32 (1987) 749–755.
[5] Y. Zhang, X. Cao, H. Yuan, W. Zhang, Z. Zhou, Int. J. Hydrogen Energy 24 (1999) 529–536.
[6] X. Wang, H. Luo, D.-R. Zhou, H. Yang, P.J. Sebastian, S.A. Gamboa, Int. J. Hydrogen Energy 29 (2004) 967–972.
[7] C. Iwakura, A. Honji, H. Tamura, Electrochim. Acta 26 (1981) 1319–1326.
[8] P. Rasiyah, A.C.C. Tseung, J. Electrochem. Soc. 130 (1983) 365–368.
[9] E.B. Castro, C.A. Gervasi, J.R. Vilche, J. Appl. Electrochem. 28 (1998) 835–841.
[10] S. Palmas, F. Ferrara, A. Vacca, M. Mascia, A.M. Polcaro, Electrochim. Acta 53 (2007) 400–406.
[11] C.R. Davidson, G. Kissel, S. Srinivasan, J. Electroanal. Chem. 132 (1982) 129–135.
[12] P. Rasiyah, A.C.C. Tseung, J. Electrochem. Soc. 130 (1983) 2384–2386.
[13] S.K. Tiwari, S. Samuel, R.N. Singh, G. Poillerat, J.F. Koenig, P. Chartiers, Int. J. Hydrogen Energy 20 (1995) 9–15.
[14] C. Bocca, A. Barbucci, M. Delucchi, G. Cerisola, Int. J. Hydrogen Energy 24 (1999) 21–26.
[15] J.P. Singh, N.K. Singh, R.N. Singh, Int. J. Hydrogen Energy 24 (1999) 433–439.
[16] R.N. Singh, J.P. Singh, B. Lal, M.J.K. Thomas, S. Bera, Electrochim. Acta 51 (2006) 5515–5523.
[17] Y. Matsumoto, S. Yamada, T. Hishida, E. Sato, J. Electrochem. Soc. 127 (1980) 2360–2364.
[18] J.O'M. Bockris, T. Otagawa, J.Phys. Chem. 87 (1983) 2960–2971.
[19] C. Bocca, G. Cerisola, E. Magnone, A. Barbucci, Int. J. Hydrogen Energy 24 (1999) 699–707.
[20] R.N. Singh, B. Lal, Int. J. Hydrogen Energy 27 (2002) 45–55.
[21] T. Kessler, J.R. Vilche, M. Ebert, K. Jüttner, W.J. Lorenz, Chem. Eng. Technol. 14 (1991) 263–269.
[22] K.K. Lian, D.W. Kirk, S.J. Thorpe, J. Electrochem. Soc. 142 (1995) 3704–3712.
[23] A.M. Fundo, L.M. Abrantes, Russian J. Electrochem. 42 (2006) 1291–1297.
[24] A.I. Krasil'shchikov, Zh. Fiz. Khim. 37 (1963) 531.
[25] N. Sato, G. Okamoto, Electrochim. Acta 10 (1965) 495–502.
[26] M.H. Miles, G. Kissel, P.W.T. Lu, S. Srinivasan, J. Electrochem. Soc. 123 (1976) 332–336.
[27] P.W.T. Lu, S. Srinivasan, J. Electrochem. Soc. 125 (1978) 1416–1422.
[28] G. Bronoel, J. Reby, Electrochim. Acta 25 (1980) 973–976.
[29] L.D. Burke, T.A.M. Twomey, J. Electroanal. Chem. 167 (1984) 285–290.
[30] B.E. Conway, T. Liu, J. Chem. Soc., Faraday Trans. 1 (83) (1987) 1063–1079.
[31] M.R. Gennero De Chialvo, A.C. Chialvo, Electrochim. Acta 33 (1988) 825–830.
[32] C. Bocca, A. Barbucci, G. Cerisola, Int. J. Hydrogen Energy 23 (1998) 247–252.
[33] L.D. Burke, M.E. Lyons, O.J. Murphy, J. Electroanal. Chem. 132 (1982) 247–261.
[34] H. Willems, A.G.C. Kobussen, J.H.W. De Wit, G.H.J. Broers, J. Electroanal. Chem. 170 (1984) 227–242.
[35] H. Willems, A.G.C. Kobussen, I.C. Vinke, J.H.W. De Wit, G.H.J. Broers, J. Electroanal. Chem. 194 (1985) 287–303.
[36] M.R. Gennero De Chialvo, A.C. Chialvo, Electrochim. Acta 35 (1990) 437–443.
[37] M.E.G. Lyons, L.D. Burke, J. Electroanal. Chem. 170 (1984) 377–381.
[38] M.E.G. Lyons, M.P. Brandon, Phys. Chem. Chem. Phys. 11 (2009) 2203–2217.
[39] R.F. Scarr, J. Electrochem. Soc. 116 (1969) 1526–1532.
[40] M.E.G. Lyons, M.P. Brandon, J. Electroanal. Chem. 631 (2009) 62–70.
[41] R.A. Robinson, R.H. Stokes, Electrolyte Solutions, Revised second ed., Butterworth & Co. Ltd., London, 1965. p. 492.
[42] J.C.K. Ho, D. Piron, J. Electrochem. Soc. 142 (1995) 1144–1149.
[43] J.C.K. Ho, D. Piron, J. Appl. Electrochem. 26 (1996) 515–521.
[44] G.W.D. Briggs in: G.J. Hills, D. Pletcher, H.R. Thirsk (Eds.), Electrochemistry – Specialist Periodical Reports, vol. 4, The Chemical Society, London, 1974, pp. 33–54.
[45] L.D. Burke, T.A.M. Twomey, J. Electroanal. Chem. 162 (1984) 101–119.
[46] J. McBreen, in: J.O. Besenhard (Ed.), Handbook of Battery Materials, Wiley-VCH, Weinheim, 1999, pp. 135–151.
[47] M. Wehrens-Dijksma, P.H.L. Notten, Electrochim. Acta 51 (2006) 3609–3621.
[48] H. Bode, K. Dehmelt, J. Witte, Electrochim. Acta 11 (1966) 1079–1087.
[49] R. Barnard, C.F. Randell, F.L. Tye, J. Appl. Electrochem. 10 (1980) 109–125.
[50] R. Barnard, C.F. Randell, F.L. Tye, J. Electroanal. Chem. 119 (1981) 17–24.
[51] W.K. Behl, J.E. Toni, J. Electroanal. Chem. 31 (1971) 63–75.
[52] H. Gomez Meier, J.R. Vilche, A.J. Arvia, J. Electroanal. Chem 134 (1982) 251–272.
[53] H. Gomez Meier, J.R. Vilche, A.J. Arvia, J. Electroanal. Chem 138 (1982) 367–379.
[54] L.D. Burke, M.M. Murphy, J. Electrochem. Soc. 138 (1991) 88–94.
[55] R.P. Šimpraga, J. Electroanal. Chem. 355 (1993) 79–96.
[56] T.-C. Liu, W.G. Pell, B.E. Conway, Electrochim. Acta 44 (1999) 2829–2842.
[57] K.E. Heusler, in: R.P. Frankenthal, J. Kruger (Eds.), Passivity of Metals, Electrochemical Soc. Inc., Princeton, New Jersey, 1978, pp. 771–801.
[58] T. Ohtsuka, N. Sato, J. Electroanal. Chem. 147 (1983) 167–179.
[59] A. Foelske, H.-H. Strehblow, Surf. Interf. Anal. 34 (2002) 125–129.
[60] G.W. Simmons, in: R.P. Frankenthal, J. Kruger (Eds.), Passivity of Metals, Electrochemical Soc. Inc., Princeton, New Jersey, 1978, pp. 899–917.
[61] R.N. Singh, J.-F. Koenig, G. Poillerat, P. Chartier, J. Electrochem. Soc. 137 (1990) 1408–1413.
[62] D. Erts, E. Ahlberg, J. Asbjörnsson, H. Olin, J. Prikulis, Appl. Phys. A66 (1998) S477–S480.
[63] L.D. Burke, M.E.G. Lyons, J. Electroanal. Chem. 198 (1986) 347–368.
[64] G. Larramona, C. Gutierrez, J. Electrochem. Soc. 136 (1989) 2171–2178.
[65] W.O'Grady, C. Iwakura, J. Huang, E. Yeager, in: M.W. Breiter (Ed.), Proceedings of the Symposium on Electrocatalysis, The Electrochemical Society Inc., Pennington, NJ, 1974, p. 286.
[66] J. Willsau, O. Wolter, J. Heitbaum, J. Electroanal. Chem. 195 (1985) 299–306.
[67] L.D. Burke, M.E.G. Lyons, D.P. Whelan, J. Electroanal. Chem. 139 (1982) 131–142.
[68] L.D. Burke, M.E. Lyons, E.J.M. O'Sullivan, D.P. Whelan, J. Electroanal. Chem. 122 (1981) 403–407.
[69] L.D. Burke, D.P. Whelan, J. Electroanal. Chem. 162 (1984) 121–141.
[70] L.D. Burke, M.E.G. Lyons, in: R.E. White, J.O'M. Bockris, B.E. Conway (Eds.), Modern Aspects of Electrochemistry, 18, Plenum Press, New York, 1986, pp. 169–248.
[71] N. Sato, Electrochemistry at Metal and Semiconductor Electrodes, Elsevier, 1998.
[72] E.J.M. O'Sullivan, L.D. Burke, J. Electrochem. Soc. 137 (1990) 466–471.
[73] J. Rossmeisl, A. Logadottir, J.K. Nørskov, Chem. Phys. 319 (2005) 178–184.
[74] J. Rossmeisl, Z.-W. Qu, H. Zhu, G.-J. Kroes, J.K. Nørskov, J. Electroanal. Chem. 607 (2007) 83–89.
[75] J.P. Hoare, The Electrochemistry of Oxygen, Interscience, New York, 1968. pp. 82–91.
[76] J.J. MacDonald, B.E. Conway, Proc. Roy. Soc. London, Ser. A 269 (1962) 419–440.
[77] R.E. Meyer, J. Electrochem. Soc. 107 (1960) 847–853.
[78] B. Beverskog, I. Puigdomenech, Corros. Sci. 38 (1996) 2121–2135.
[79] A. Damjanovic, A. Dey, J.O'M. Bockris, Electrochim. Acta. 11 (1966) 791–814.
[80] L.D. Burke, E.J.M. O'Sullivan, J. Electroanal. Chem. 117 (1981) 155–160.
[81] L.D. Burke, M.I. Casey, V.J. Cunnane, O.J. Murphy, T.A.M. Twomey, J. Electroanal. Chem. 189 (1985) 353–362.
[82] M.M. Lohrengel, J.W. Schultze, Electrochim. Acta. 21 (1976) 957–965.
[83] S. Trasatti, O.A. Petrii, Pure Appl. Chem. 63 (1991) 711–734.
[84] B.E. Conway, P.L. Bourgault, Can. J. Chem. 37 (1959) 292–307.
[85] A.I. Fedorova, A.N. Frumkin, J. Phys. Chem. USSR 27 (1953) 247–249.
[86] J. O'M. Bockris, T. Otagawa, J. Electrochem. Soc. 131 (1984) 290–302.
[87] J. O'M Bockris, S.U.M. Khan, Surface Electrochemistry, A Molecular Level Approach, Plenum, New York, 1993. p. 291.